Multiaxial Non-proportional Low Cycle Fatigue Properties of HIPped A319 Cast Aluminum Alloy

B. Ge[1,2], X.S. Liu[1,2], G.Q. He[1,2], P.W. Le[1,2], Z.Q. Zhou [1,2], J.Q. Pan [1,2], Z.A. Huang [1,2], J.Q. Li [1,2], Q.G. Wang[3]

1, School of Material Science and Engineering, Tongji University, Shanghai 201804, China
2, Shanghai Key Laboratory for R&D and Application of Metallic Functional Materials, Shanghai 201804, China
3, Materials Technology, Global Product Group, General Motors Co., Pontiac, MI 48340, USA

Abstract

This paper describes a microstructure-based multiaxial non-proportional fatigue life prediction model with maximum shear strain and non-proportionality as damage parameters applied to A319 alloy. The materials made with different casting cooling rates and Sr modification are characterized and quantified in terms of secondary dendrite arm spacing (SDAS), size and aspect ratio of eutectic Si particles. Multiaxial non-proportional fatigue tests have been performed on six groups of A319 alloys to systematically analyze the effect of microstructure and loading path on the fatigue properties of Al-Si cast alloy. The first part of the paper is focused on microstructure quantitative characterization to determine the influence of different casting conditions, followed by stress response behavior and fatigue fracture analysis. Finally, quantitative relationship between six fatigue life parameters and microstructure characteristics is established and a new fatigue life prediction model is proposed to predict fatigue life of Al-Si alloy under multiaxial non-proportional loading condition.

Keywords: A319 aluminum alloy, multiaxial non-proportional fatigue, fatigue parameters, life prediction

1 Introduction

Al-Si cast alloy has become an alternative structure material to replace steels in many industrial applications due to its light weight, high corrosion resistance and comprehensive mechanical properties. However, practical application scenarios have put forward high requirements for the fatigue performance of Al-Si cast alloy, and a significant amount of related researches had been performed in the last few decades. [1-5]

The fatigue properties of Al-Si cast alloys are controlled by multiscale microstructures like secondary dendrite arm spacing (SDAS), Si particles, intermetallic and casting defects which are determined by various casting processes and melt treatment. Haskel's [6] research showed that A356 aluminum alloy has better performance under low cycle fatigue due to the strength of the matrix strengthened by Mg_2Si after T6 heat treatment. Tenkamp et al [7] investigated the effect of degassing with nitrogen and hot isotactic pressing (HIP) on the fatigue properties of aluminum alloy and the microscopic observation results showed that degassing and HIP had no obvious effect on the size, morphology and distribution of silicon particles, grain size and SDAS, but the porosity of the material is significantly reduced, thus improving the fatigue strength of the alloy. Kumai et al [8] pointed out that degassing and HIP can eliminate the influence of porosity and aluminum alloy can be considered pore−free after the treatment. Under this circumstance, the fatigue property of Al-Si cast alloy is strongly dependent on SDAS, morphology and distribution of eutectic Si particles, which are decided by casting cooling rate and modification treatment. However, most of the existing studies only focused on the effect of cooling rate and modification on the microstructure or uniaxial fatigue life of materials, and the effects of SDAS and silicon particles with different sizes and distributions on the cyclic deformation and

fatigue fracture characteristics of materials are insufficient, especially under the condition of multiaxial non-proportional fatigue loading. In addition, there are few studies that involve the contrast of effect of casting cooling rate and modification treatment on fatigue properties of Al-Si cast alloys. [9-16]

To better enhance the practical application of materials in industrial applications and avoid time-consuming fatigue testing as much as possible, fatigue life prediction is another field researcher has focused on. Morrow [17] first proposed the energy method, and considered that the main reason of fatigue failure was the accumulation of plastic work, which led to irreversible damage of materials. Ellyin et al [18] first used the total strain energy density to fit the multiaxial fatigue life. After that, Garud et al [19] further developed the plastic work theory and extended it to multiaxial fatigue. Although the energy method can well predict the multiaxial non-proportional fatigue life, the energy is an abstract scalar and can not describe the plane and direction of crack initiation and propagation under cyclic loading; After studying a large number of multiaxial fatigue data, Brown and Miller [20] concluded that two strain parameters should be needed to describe the fatigue process, i.e. the cyclic shear strain and normal strain on a special plane, and proposed KBW model based on maximum shear strain, which is the so-called critical plane method. Socie et al [21] considered the influence of mean stress and modified the model with mean stress. The direction of crack propagation is considered in the application of the critical plane method, so it has certain physical significance. However, it is not suitable for high stacking fault energy materials, like cast aluminum, and it also needs accurate cyclic constitutive equation. These two points limit the application of this method to a certain extent. Manson-Coffin-Basquin model (MCB) is another mainstream fatigue life prediction method based on total strain:

$$\frac{\Delta\varepsilon_t}{2}=\frac{\Delta\varepsilon_e}{2}+\frac{\Delta\varepsilon_p}{2}=\frac{\sigma_f^{'}}{E}(2N_f)^b+\varepsilon_f^{'}(2N_f)^c \quad (1)$$

where E is elastic modulus, N_f is the number of cycles to fatigue failure, $\frac{\Delta\varepsilon_t}{2}$ is total

strain amplitude, $\frac{\Delta\varepsilon_e}{2}$ is elastic strain amplitude, $\frac{\Delta\varepsilon_p}{2}$ is plastic strain amplitude, $\sigma_f^{'}$ is fatigue strength coefficient, b is fatigue strength exponent,$\varepsilon_f^{'}$ is fatigue ductility coefficient, and c is fatigue ductility exponent. Obtaining the effective fatigue parameters, is a critical step of the application of Manson-Coffin-Basquin method. Some studies flexibly used some mechanical properties of materials like tensile properties and hardness of materials to estimate the fatigue parameters in MCB method. However, none of these studies have ever touched the key factors that decided the properties of the materials, namely microstructure, and few studies extended the MCB method to multiaxial field effectively.

In this article, the authors performed fatigue experiments on A319 casting aluminum alloy with different cooling rates and Sr modification treatment under 3 multiaxial non-proportional loading paths, systematically analyzed the influence of SDAS, Si particles and different loading paths on fatigue properties of Al-Si cast alloy, and established a new microstructure-based multiaxial non-proportional fatigue life prediction model.

2 Experimental procedure

2.1 Material preparation

The experimental material was A319 aluminum alloy with the following chemical composition (wt%): Si 6.2, Fe 0.54, Cu 3.4, Mn 0.25, Mg 0.3, Ni 0.25, Zn 0.8, Sn 0.1 and Al (balance). Prior to casting, the molten metal was degassed using Argon for at least 30 min to decrease the hydrogen level to less than 0.15ml/100g Al. The hot isostatic pressing (HIP) treatment was conducted at 540°C and 100 MPa for 2 hrs. The eutectic modification was performed by adding 150-ppm strontium (Sr) to the molten metal with Al-10 wt.% Sr master alloy. Precision sand casting molds with

an end chill were used to make plate castings. The end chill was a copper block sitting at the bottom of sand molds, leading to high cooling rate near the chill (~10 °C·s^{-1}), a slow cooling rate far away from the chill (~0.1 °C·s^{-1}) and a middle cooling rate (~1 °C·s^{-1}) in the middle of these two areas.

Before being machined into fatigue specimens, the blanks were heat-treated to T6 condition: solution treated at 480°C for 7.5 hrs in an air circulated furnace, quenched in warm water (approximately 60°C) followed immediately by artificial aging at 240°C for 1h, and then cooling in air to room temperature.

According to different cast conditions shown in Table 1, six batches of specimens with various degrees of microstructure were obtained.

Table 1 Different cast conditions of specimens

Specimen	Sr modification	Cooling rate
A319+Sr+High	Yes	10°C·s^{-1}
A319+Sr+Mid	Yes	1°C·s^{-1}
A319+Sr+Low	Yes	0.1°C·s^{-1}
A319+um+High	No	10°C·s^{-1}
A319+um+Mid	No	1°C·s^{-1}
A319+um+Low	No	0.1°C·s^{-1}

2.2 Microstructural quantification

Quantification of key microstructure characteristics including SDAS, Si particle sizes and aspect ratios was conducted by using an optical microscope and software Image-Pro Plus.

The size of Si particles was defined as the square root of the area of the particles ($\sqrt{area}$) on metallographic section, and aspect ratio of a Si particle referred to the ratio of maximum value to minimum value between two points at the boundary of the particle. More than 500 particles were measured for each specimen. The value of SDAS was measured using the linear intercept method.

2.3 Mechanical testing

2.3.1 Tensile testing

The tensile tests were conducted at room temperature on a MTS809 test system at a strain rate of $10^{-3}s^{-1}$. The strain was measured by an extensometer attached to the specimen gauge section. The tensile test specimens were machined in accord with ISO 6892-1-2009 standard, and at least two specimens were tested for each condition.

2.3.2 Fatigue testing

After heat treatment, the blanks cut from casting plates were machined into fatigue bars and the geometry and dimensions of which are shown in Fig.1. Both uniaxial fatigue and multiaxial non-proportional fatigue tests were performed using a MTS809 Axial/Torsional test system, the strain ratio (R) was -1, the frequency was 1hz, and the remaining experimental variables can be seen in Table.1. An extensometer was used to measure longitudinal strain of specimens. For each condition three specimens were tested and the average values are presented in this paper. It should be noted that uniaxial fatigue tests performed under 5 strain amplitudes were only used for the calculation of fatigue parameters, and no further related analysis is shown in the following parts of this article.

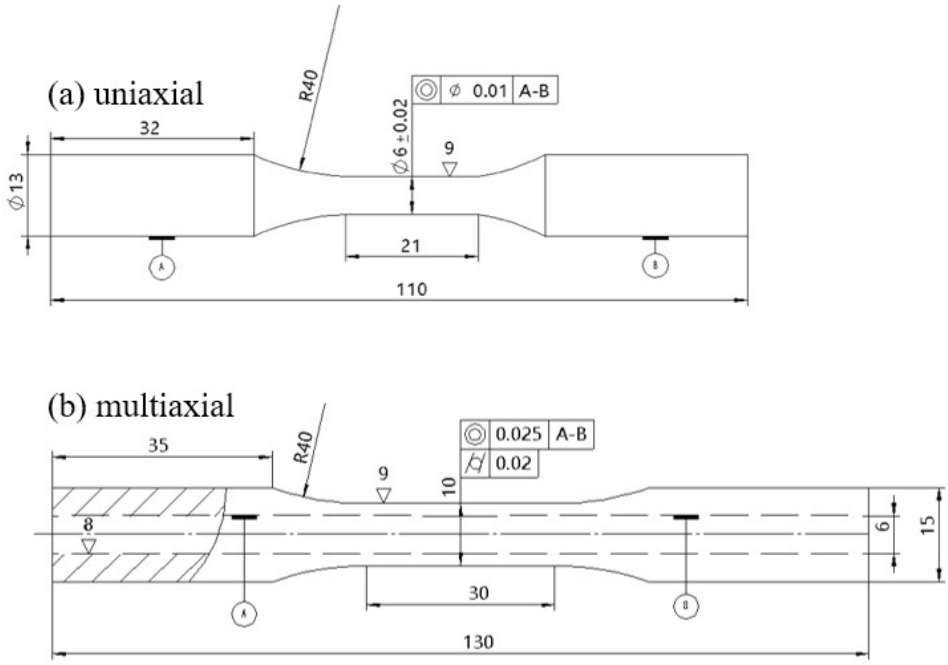

Fig.1 Geometry and dimensions of fatigue specimens (units: mm)

Table.1 Experimental parameters of fatigue tests

Path		$\Delta\varepsilon_t/2$	$\varepsilon_1/\varepsilon_3$
Uniaxial	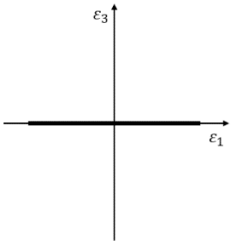	0.20%, 0.25%, 0.30%, 0.35%, 0.40%	/
Diamond	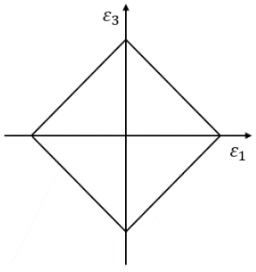	0.25%	1

Square	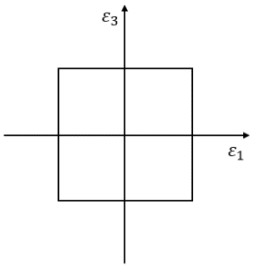	0.25%	1
Rectangular	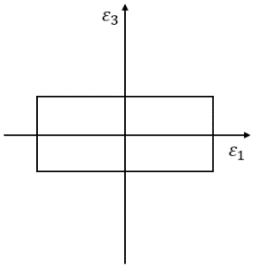	0.25%	2

2.4 Fractographic Analysis

For fractography analysis, all fatigue specimens were evaluated by examining fracture surfaces with a scanning electron microscope (SEM).

3. Results and discussion

3.1 Quantitative characterization of microstructure

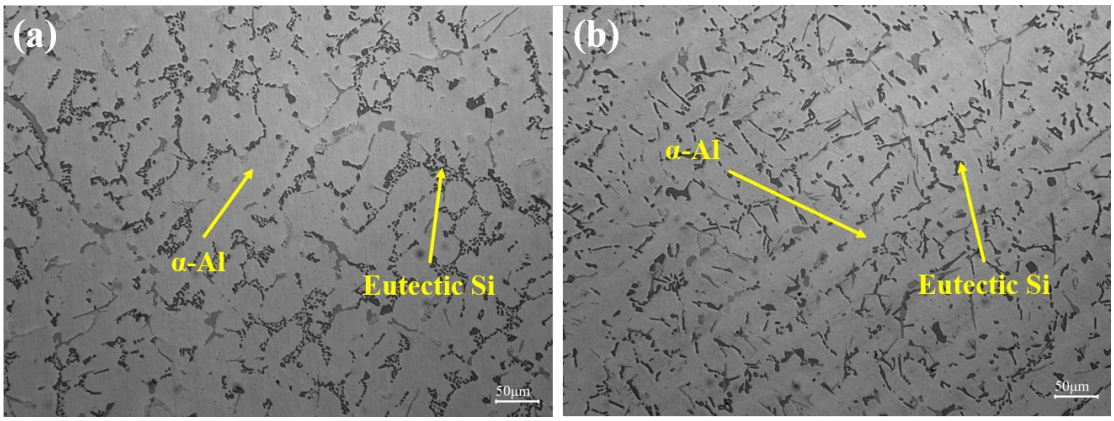

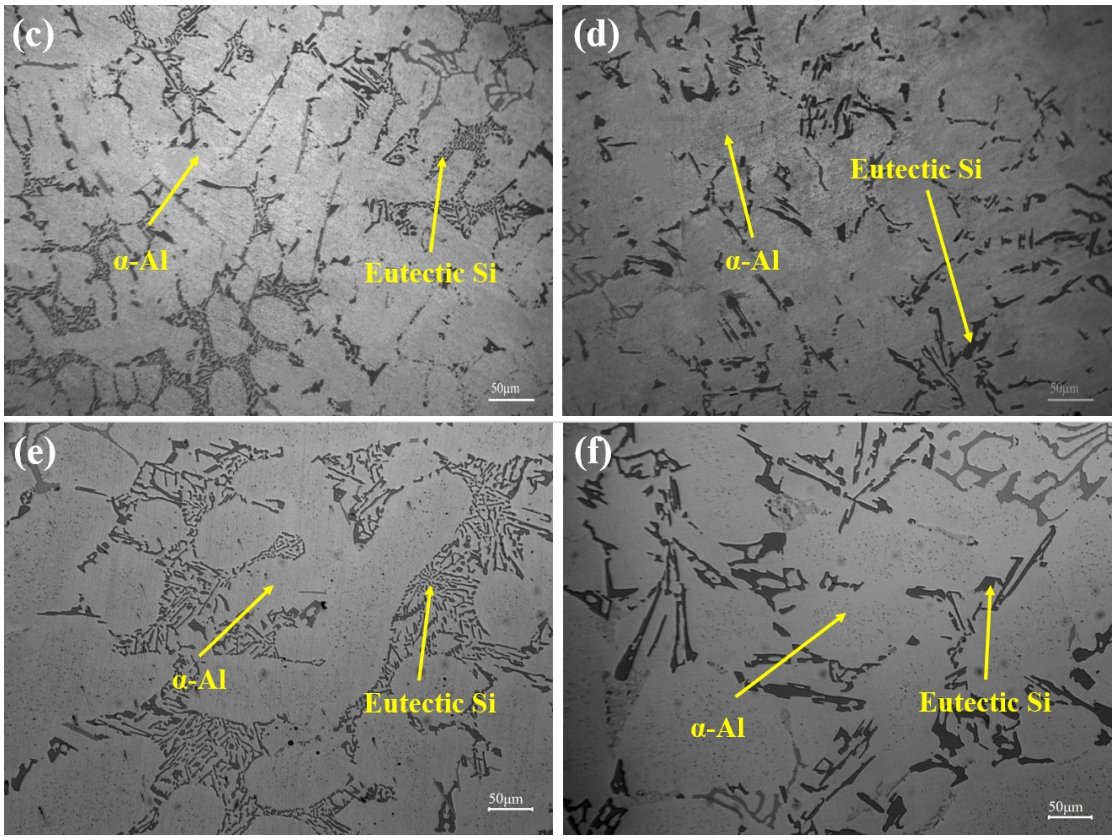

Fig.2 OM images of A319 alloys: (a)A319+Sr+High; (b) A319+um+High; (c) A319+Sr+Mid; (d) A319+um+Mid; (e) A319+Sr+Low; (f) A319+um+Low

Fig. 2 presents the typical metallographic images of A319 aluminum alloy with different casting and melt treatment conditions. It can be seen that after T6 heat treatment, no overheating or incipient melting is found in all specimens, meeting the requirement of JB/T 7946.1~7946.4-1999 standard. The material is mainly composed of α-Al phase and dark gray eutectic Si phase. α-Al dendrites are separated by Si particles with different morphologies, forming different metallographic structure distribution, considering the different moduli of α-Al and Si particles, this will inevitably cause the change of the mechanical properties of the material. Besides, no obvious shrinkage or gas porosity can be found in all specimens after HIPing and degassing.

The effect of solidification cooling rate and Sr modification on the secondary dendrite arm spacing (SDAS) and Si particles is very pronounced in cast aluminum alloys. The higher the cooling rate, the smaller the dendrite arm spacing. This is because the high cooling rate reduces the solute diffusion rate and distance and the

secondary dendrite has no enough time to grow. The high cooling rate can also refine the Si particles. Compared with the unmodified specimens, the addition of Sr can effectively improve the morphology of eutectic Si from coarse acicular like to fibrous or spherical particles, and make the distribution more dispersed and uniform. The existence of Sr can also reduce the solid-liquid interface energy of α-dendrite, decrease the growth undercooling degree of dendrite tip, inhibit the nucleation of equiaxed crystal in liquid phase, and make SDAS and primary dendrite spacing decrease with the increase of Sr content. The detailed quantitative measurement results of microstructure characteristics are shown in Table. 2.

Table.2 Quantitative results of metallographic analysis

Specimen	SDAS(μm)	Asp $_{Si}$	Size $_{Si}$ (μm)
A319+Sr+High	17.57±1.89	1.72±0.18	3.21±0.52
A319+Sr+Mid	52.23±2.54	2.27±0.21	3.35±0.38
A319+Sr+Low	72.63±5.53	2.34±0.24	3.43±0.41
A319+um+High	24.26±2.36	3.12±0.21	6.03±1.26
A319+um+Mid	58.17±3.44	3.41±0.14	10.97±1.04
A319+um+Low	68.50±5.72	3.51±0.34	11.24±1.64

Table. 3 shows the tensile properties of the specimens with different solidification cooling rates and the Sr-addition. It is seen that the materials with higher cooling rate have higher strength and better ductility. Addition of Sr further improves the strength and plasticity.

Table.3 Tensile properties of A319 alloys

Specimen	E(GPa)	YS(MPa)	UTS (MPa)	δ (%)
A319+Sr+High	74.796	249.046	314.611	2.460
A319+Sr+Mid	75.962	221.202	300.104	2.112
A319+Sr+Low	76.249	215.623	226.883	2.433
A319+um+High	75.598	204.725	274.618	2.515

A319+um+Mid	76.042	210.631	254.636	1.786
A319+um+Low	76.127	201.631	219.632	1.413

3.2 Fatigue properties

3.2.1 Cyclic stress response under a given strain amplitude

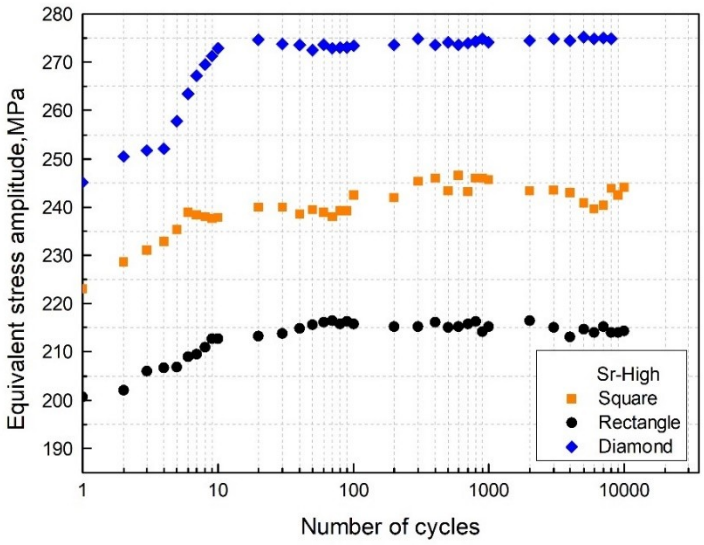

Fig.3 Cyclic stress amplitude response of A319 alloys under a strain amplitude of 0.25% with different loading paths

Fig. 3 presents the change of cyclic stress amplitude as a function of number of cycles under a strain amplitude of 0.25% with three loading paths. It can be seen that A319 cast aluminum alloy shows similar cyclic hardening characteristics under three loading conditions. The proliferation and interaction of dislocation in Al matrix results in a large number of dislocation entanglement and interweaving phenomenon. As the cyclic loading proceeds, the dislocation structure becomes more and more evident. Moreover, the pinning effect of these interlaced dislocation structures on the newly formed dislocations becomes more significant, which seriously hinders the dislocation movement. Under this influence, the critical stress to form new dislocations increases,

which leads to the increase of cyclic stress amplitude. Under the same equivalent strain amplitude, the higher the stress amplitude after cyclic stability the greater the deformation resistance of material. As shown in Fig. 3, the hardening rate is higher in the initial stage of cyclic loading under the diamond loading path, and the stress amplitude after cyclic stabilization is the largest among the three loading paths. Under the condition of non-proportional cyclic loading, the direction of the maximum shear stress plane changes periodically, and the preferred slip system changes synchronously, resulting in additional dislocation slip. Longer hardening process refers to more fatigue damage accumulation. In the diamond loading path, whether axial or torsional, the effective strain of the material in the same cycle is greater than that of the square loading path and the rectangular loading path. The initial cyclic hardening rate of the square loading path and the rectangular loading path is obviously lower than that of the diamond loading path. Since the maximum strain of the rectangular loading path in torsion direction is only half of that in axial direction, it has the lowest stress response amplitude after reaching the stable stage.

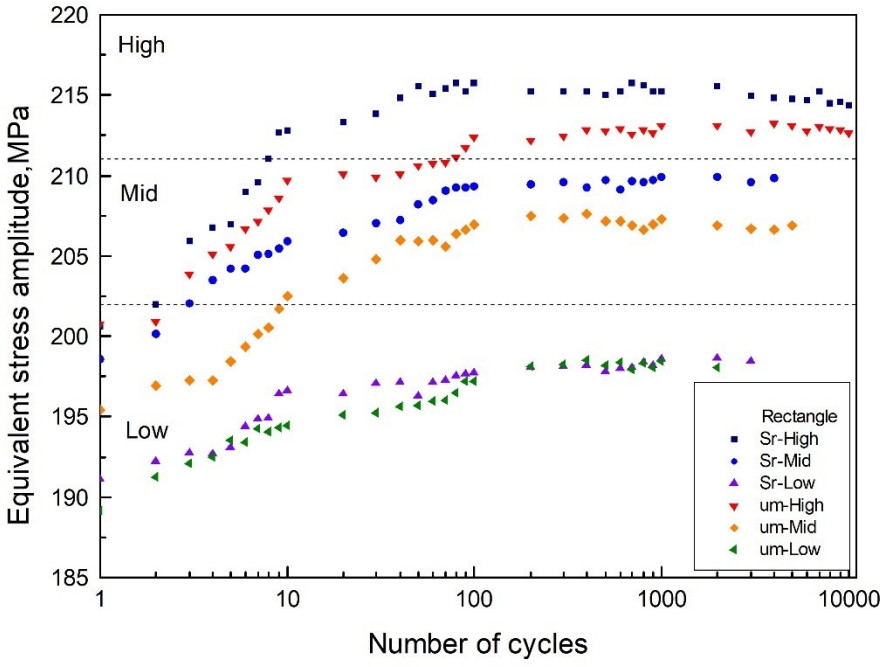

Fig.4 Cyclic stress response of A319 alloy with different microstructure combinations under a given effective strain amplitude 0.25%?

Fig. 4 shows the variation of equivalent stress amplitude of A319 cast aluminum alloy with different microstructure combinations under rectangular loading path. There are a lot of obstacles such as eutectic Si particles, second-phase particles and slip bands in the alloy, which lead to dislocation stacking. With the development of cyclic deformation, the dislocation density continues to increase, and the interaction between dislocations and the obstacles mentioned above becomes more and more intensive, which causes the material to undergo cyclic hardening. It can be seen that under the same loading conditions the cyclic hardening phenomenon occurs in every specimen, and the cyclic stability is achieved after a certain number of cycles. Specimens with high cooling rate and Sr modification have the maximum stress amplitude after reaching the stable stage, showing a very fast hardening rate compared with other specimens in the initial stage of cyclic loading. From the perspective of modification, the equivalent stress amplitude of the specimens with the same cooling rate after Sr modification will increase slightly. Comparing specimens A319+Sr+Mid and A319+um+High, it can be found that although the Si particles are modified in the specimen of A319+Sr+Mid, the stress amplitude of stable cycles is still lower than that of A319+um+High, which indicates that Sr modification in this study is not enough to make up the difference by cooling rate. For specimens A319+Sr+Low and A319+um+Low, due to the lowest solidification cooling rate, the cyclic hardening phenomenon of both samples is not as obvious as other specimens. Although the Sr-modified sample (A319Sr_Low) shows slightly higher cyclic hardening in the early stage of cycles than the unmodified one, no obvious difference is seen between both samples in the overall stress response.

3.3 Fractography analysis

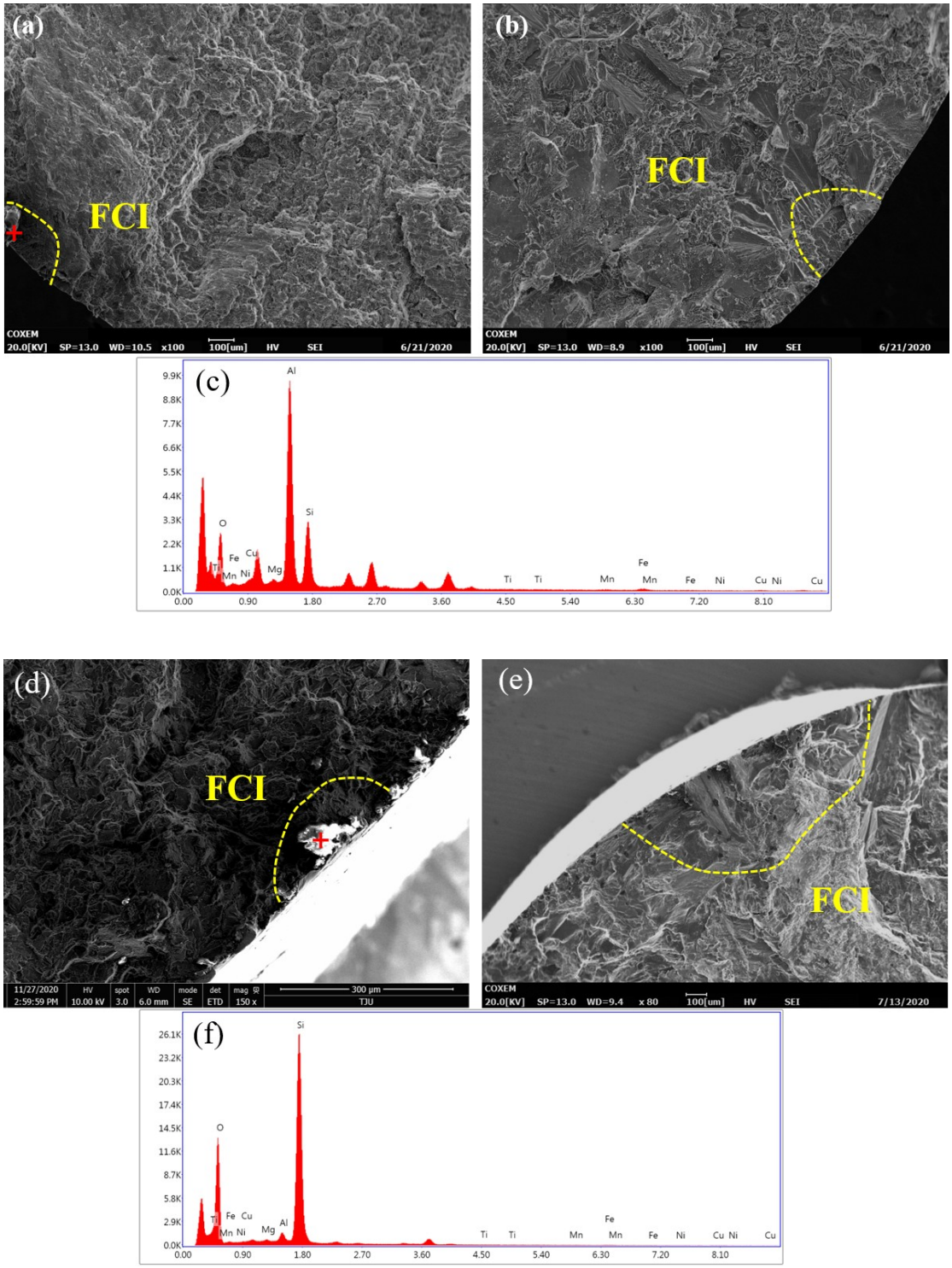

Fig.5 Typical SEM images of fracture surface of A319 alloy: (a) Diamond loading path A319+Sr+High ; (b) Diamond loading path of A319+Sr+Low ; (c) EDX analysis of '+' area in

(a); (d) Square loading path of A319+um+High ; (e) Square loading path of A319+um+Low; (f) EDX analysis of '+' area in (d);

The fatigue crack initiation regions (FCI) of A319 alloys with different cooling rates are shown in Fig.5. The area surrounded by the yellow dotted line is the crack initiation source. It can be seen that all the crack initiators are located on the surface or near the surface of the specimen. Because of the effect of DG and HIPing, the fatigue crack initiation from the surface porosity is avoided. Oxide inclusions with star shaped radiation pattern act as the crack initiation sources at the edge in the specimen with higher cooling rate, while the crack initiation zone of A319 aluminum alloy at low cooling rate originate from the secondary phase particles. The fracture surfaces of specimens with low cooling rate are also very rough and uneven, and the fatigue bands often gather in divergent directions.

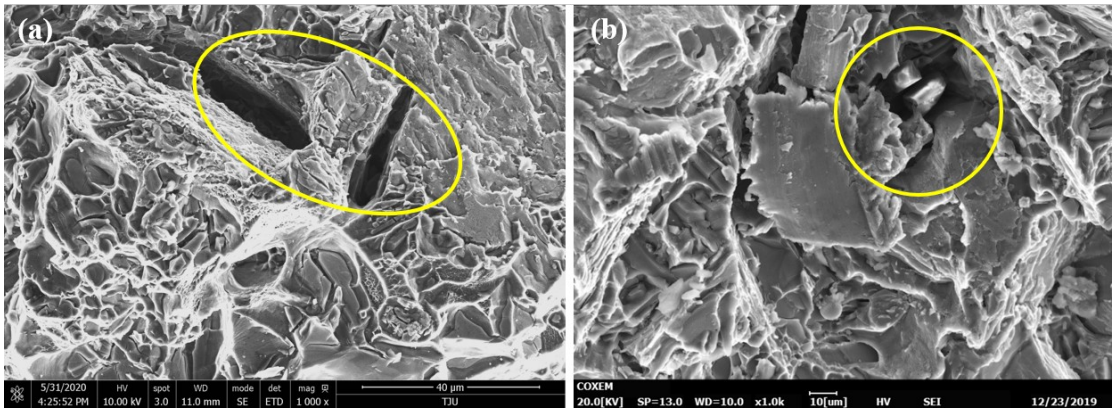

Fig.6 Typical SEM images of fracture surface of A319 alloy:

(a) Square path A319+Sr+High ; (b) Square path A319+um+High

Because of the different plasticity of eutectic Si and aluminum matrix and the combined effect of tension and torsion stresses, Si particles preferentially fracture and form crack initiators. In addition, the interface between eutectic Si and aluminum matrix is a non-coherent interface with vacancy defects, leading to interface separation and forming crack initiators. Fig. 6 shows the steady-crack-propagation (SCP) zone of A319 cast aluminum alloy with different Sr modification conditions under square loading path. In Fig. 6 (a), the pits left by two Si particles can be clearly

seen. It can be inferred that the Si particles are fine fibers before debonding. The interface separation between Si particles and aluminum matrix does not cause obvious damage to the surrounding morphology, while the Si particles perpendicular to the fracture surface in Fig. 6 (b) are more seriously damaged.

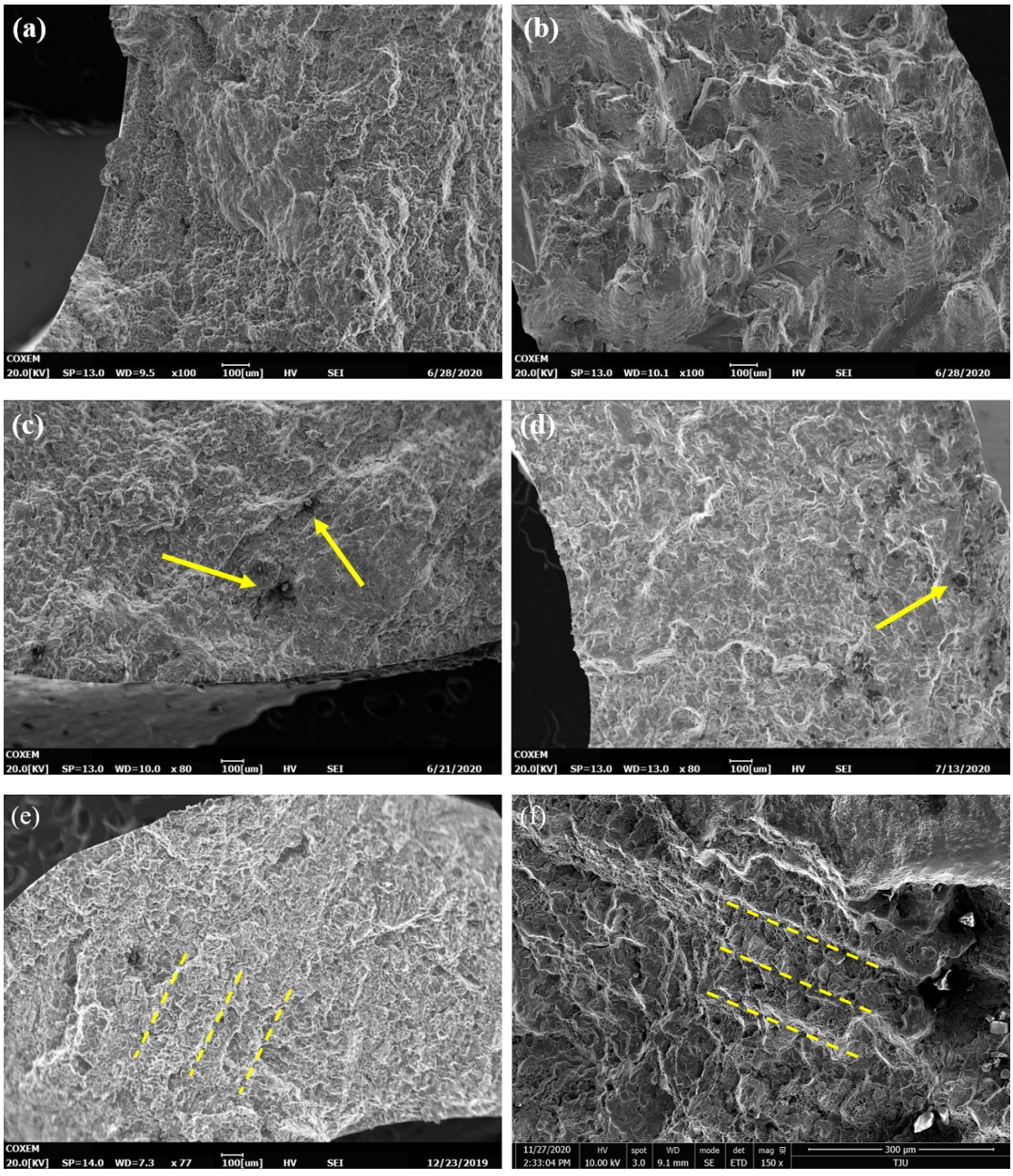

Fig.7 Typical SEM images of fracture surfaces of A319 alloy: (a)Rectangular loading path of A319+Sr+High; (b)Rectangular loading path of A319+Sr+Low; (c)Diamond loading path A319+Sr+High; (d)Rectangular loading path A319+um+High; (e)Square loading path

A319+um+High; (f)Diamond loading path A319+Sr+High

The fast-fracture zone is resulted from quasi-static fracture mechanism, and its property is close to tensile failure. Fig. 7 shows the morphology of final fracture zone of A319 cast aluminum alloys. It has the following characteristics: first, this part of the area is very rough, as shown in Fig. 7 (a), (b). In addition, it can be seen from the Fig.7 (a) and (b) that the roughness of the two specimens is different due to the difference of solidification cooling rate. Under the same magnification, the high cooling rate specimen presents fine continuous fluctuation, while the low cooling rate specimen shows rough block undulation; Secondly, oxide inclusions are observed in some samples, as shown in Fig. 7 (c), (d); Lastly, some parallel tearing prisms can be seen in the final fracture zone, as shown in Fig. 7 (e), (f).

3.4 Life model for multiaxial non-proportional fatigue

It is well known that the fatigue behavior and fatigue life of Al-Si alloy are affected by the cast defects, especially porosity. With the increasing of porosity, the fatigue life decreases. In this study, degassing and HIPing were employed to eliminate the influence of porosity and specimens can be considered pore-free after the treatment. Because of the absence of cast defects, the fatigue life of A319 alloy is strongly dependent on the SDAS, morphology and distribution of eutectic Si particles. Therefore, developing a fatigue life prediction model based on SDAS and Si particles is practicable under this circumstance. To do so, calculation of fatigue life parameters and development of quantitative relationship between fatigue parameters and microstructural characteristics is needed..

3.4.1 Calculation of fatigue parameters

According to Manson-Coffin-Basquin (MCB) model, total strain amplitude can be divided into two parts, namely elastic strain amplitude and plastic strain amplitude,

as shown in Eq. (2) to (3). Four uniaxial fatigue parameters can be obtained by taking the logarithm of two sides of equations to get the Eq. (4) to (5) and linear regression analysis according to the corresponding strain amplitude and fatigue life.

$$\frac{\Delta\varepsilon_e}{2}=\frac{\sigma_f^{'}}{E}(2N_f)^b \tag{2}$$

$$\frac{\Delta\varepsilon_p}{2}=\varepsilon_f^{'}(2N_f)^c \tag{3}$$

$$\log ¿ \tag{4}$$

$$\log ¿ \tag{5}$$

Different from uniaxial fatigue, under multiaxial non-proportional fatigue loading, the maximum shear stress plane continuously rotates, resulting in complex dislocation structures in different directions. The complex interaction between these dislocation structures makes multiaxial non-proportional fatigue have additional hardening or strengthening phenomenon under the same equivalent stress amplitude compared to uniaxial fatigue. Therefore, the Manson-coffin model under uniaxial condition cannot be used for multiaxial fatigue life prediction. To solve this problem, He et al. [22] defined a new fatigue life prediction model by adding a series of multiaxial nonproportional fatigue parameters and taking the maximum shear strain amplitude and non-proportional degree as fatigue damage parameters:

$$\frac{\Delta\gamma_{max}}{2}=\left(1+L_2\varnothing\right)^{\frac{-1}{n^{'}}}\left(1+\upsilon_p\right)\varepsilon_f^{'}\left(2N_f\right)^{c_0}+\frac{\sigma_f^{'}}{E}\left(1+\upsilon_e\right)\left(2N_f\right)^{b_0} \tag{6}$$

where, $\frac{\Delta\gamma_{max}}{2}$ is the maximum shear strain amplitude, L_2 is the non-proportional additional strengthening coefficient, which is one of the important differences from the uniaxial fatigue life model, and its calculation method is as follows:

$$L_2=\frac{\sigma_{np}-\sigma_p}{\sigma_p} \tag{7}$$

where, σ_{np} is the equivalent stress amplitude of the material after cyclic stabilization under the circular path, σ_p is the stress amplitude after cyclic stabilization under

uniaxial or multiaxial proportional loading with the same strain amplitude. ∅ is an empirical constant related to multiaxial strain path: 0.675 for diamond path, 0.67 for square path and 0.6 for rectangular path. υ_e and υ_p are elastic Poisson's ratio and the plastic Poisson's ratio, which are 0.3 and 0.5 respectively. n' is the cyclic hardening index, which is basically consistent with uniaxial cyclic hardening index in numerical value. Therefore, it is calculated by Hollomon Equation according to uniaxial fatigue data

$$\frac{\Delta\sigma}{2}=K'\left(\frac{\Delta\varepsilon_p}{2}\right)^{n'} \quad (8)$$

where $\frac{\Delta\sigma}{2}$ is uniaxial strain amplitude, K' is cyclic strengthening coefficient, and $\frac{\Delta\varepsilon_p}{2}$ is plastic strain of the material under cyclic stable cycles. According to the above calculation method, the multiaxial fatigue parameters needed in this study are calculated and presented in Table.5:

Table.5 Fatigue paramters of A319 aluminum alloy

Specimens	σ_f'	b_0	ε_f'	c_0	L_2	n'
A319+Sr+High	845.0	-0.1487	0.7825	-0.8778	0.530	0.4940
A319+Sr+Mid	595.4	-0.1283	0.4239	-0.7481	0.520	0.2750
A319+Sr+Low	512.9	-0.1174	0.1675	-0.7636	0.310	0.1467
A319+um+High	801.2	-0.1377	0.4923	-0.7224	0.494	0.1695
A319+um+Mid	561.4	-0.1249	0.2032	-0.6124	0.350	0.1627
A319+um+Low	389.9	-0.0976	0.1092	-0.5274	0.280	0.1006

3.4.2 Fatigue life and Constitutive equation prediction

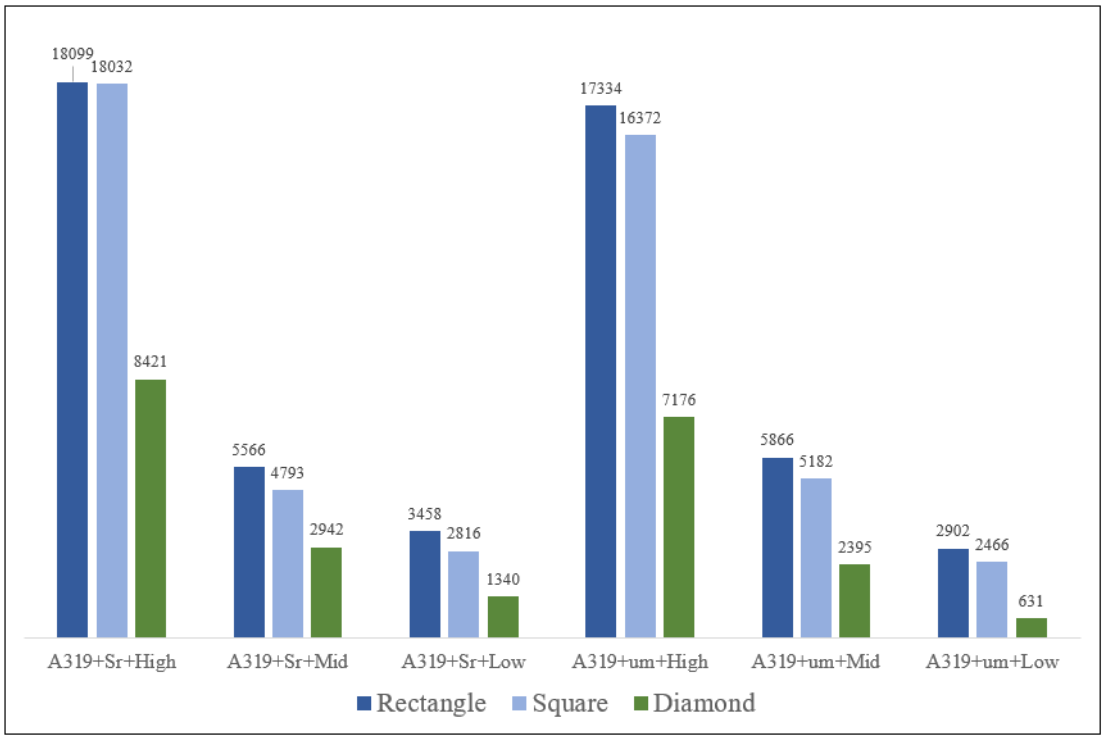

Fig.8 Fatigue life of A319 alloy

Fig. 8 shows the fatigue lives of six groups of specimens under three different loading paths when the equivalent strain amplitude is 0.25%. It can be seen that higher cooling rate leads to longer fatigue life, and the life of each specimen is also improved in various degrees after Sr modification. No matter which loading path is, the fatigue life of specimens with higher cooling rate and with Sr modification is always higher than specimens with lower cooling rate and no Sr-modification. From the perspective of path, the fatigue life of specimens under rectangular path is a little bit longer than that of square path, and the fatigue life under diamond path with larger strain amplitude axial and intorsion direction is the shortest.

Before establishing a multiaxial non-proportional fatigue life model based on microstructure, it is necessary to evaluate the reliability of the fatigue life parameters directly calculated through the uniaxial and multiaxial fatigue test data. Substituting the fatigue parameters into the above fatigue life prediction equation can obtain prediction results of constitutive equation under three multiaxial non-proportional

loading conditions.

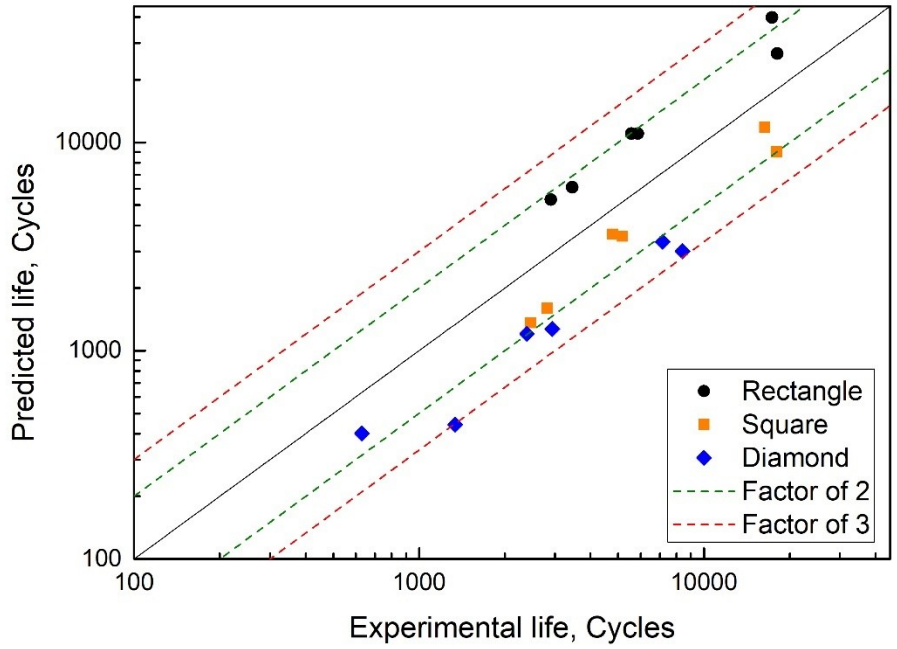

Fig.9 Prediction result of the multi-axial fatigue life based on the fatigue constitutive equation

Fig.9 shows the prediction results of the multiaxial fatigue life of A319 cast aluminum alloy based on the fatigue constitutive equation. Considering extra fatigue parameters and the complex loading state of the material under the multiaxial non-proportional, there is some decline of accuracy of prediction compared to uniaxial condition. [23] However, it can be seen from the figure that there is still a high degree of accuracy, 72% of the data points are included in the bound lines of factor of 2, and all data points fall within the bound lines of factor of 3, which proves that the calculation of each fatigue parameter is reasonable accurate, A319 cast aluminum alloy has high applicability for this method under current preparation process conditions.

3.4.3 Microstructure-based life prediction model for multiaxial non-proportional fatigue

According to our research reported earlier [23], there is an inherent quantitative

relationship between the size and aspect ratio of eutectic Si particles. Based on SDAS and the size and aspect ratio of Si particles, a quantitative relationship between microstructure and multiaxial fatigue parameters was established. The result is shown in Equation (9-14), and the equation constants are shown in Table 6.

$$\sigma_f^{'} = k_1 + k_2 * SDAS + k_3 * ¿¿3 R^2 = 0.9815 ¿ \quad (9)$$

$$b^0 = h_1 + h_2 * SDAS^2 + h_3 * ¿ R ¿^2 = 0.9212 \quad (10)$$

$$\varepsilon_f^{'} = u_1 + u_2 * SDAS + u_3 / ¿¿2 R^2 = 0.9589 ¿ \quad (11)$$

$$c^0 = v_1 + v_2 * SDAS + v_3 / ¿ R^2 = 0.9592 ¿ \quad (12)$$

$$n^{'} = t_1 * SDAS^{t_2} * ¿¿ t_3 R^2 = 0.8589 ¿ \quad (13)$$

$$L_2 = w_1 + w_2 / SDAS + w_3 * ¿ R ¿^2 = 0.4838 \quad (14)$$

Table.6 Constants in fitting equations

Constant	Value	Constant	Value
k_1	975.7	h_1	-0.1524
k_2	-6.9844	h_2	7.209E-6
k_3	-0.03235	h_3	0.0009737
u_1	0.7328	v_1	-0.6382
u_2	-0.009441	v_2	0.002271
u_3	1.750	v_3	-0.8729
t_1	6.5311	w_1	0.4775
t_2	-0.5933	w_2	2.9536
t_3	-0.7926	w_3	-0.0188

Generally, fatigue strength coefficient $\sigma_f^{'}$ is considered to be approximately equal to fracture true stress, and fatigue ductility coefficient $\varepsilon_f^{'}$ is equal to fracture true

strain, these two parameters can reflect the strength and ductility of material to a certain degree. According to Song et al [24], fatigue strength exponent b^0 ranges from −0.07 to −0.15 and fatigue plastic exponent c^0 ranges from −0.5 to −0.7 for most metallic materials. High $|b^0|$ value means high strength, and high $|c^0|$ value indicates good plasticity. In Equation (9), if SDAS is used as an independent variable to derive the two sides of the equation, it can be found that σ_f' is inversely proportional to SDAS, that is, the increase of SDAS will lead to an decrease in the value of σ_f', that is, a decrease in material strength; Similarly, it can be concluded that reducing SDAS and Si particle sizes leads to the increase of σ_f', ε_f', $|b^0|$ and $|c^0|$, representing higher strength and better plasticity of the material

The value of SDAS depends on the combined effect of casting cooling rate and Sr modification. The addition of Sr changes the morphology of eutectic Si particles from blocky flakes to fine and fibrous structure. High cooling rate ensures the greater the degree of undercooling during crystallization process, leading to greater the number of grains of the material, and the reduction of SDAS. In this case, when deformation occurs, the plastic deformation will be evenly shared among more grains, which will increase the strength and plasticity at the same time. In the process of fatigue loading, a large number of tortuous grain boundaries in the high cooling rate sample form an effective barrier to fatigue cracks. This process reduces the rate of crack growth and prolongs the fatigue life of the material. The size and morphology of Si particles are larger in specimens that have not undergone Sr modification. The thick needles are gathered around the dendrite arms. Due to the different modulus of the aluminum matrix and the Si particles, deformation is more likely to cause stress concentration around the Si particles and make them fracture or break away from the matrix. Si particles with large sizes and long axis direction perpendicular to the crack propagation plane are more likely to fracture and form micro-cracks and join with

other micro-cracks to accelerate the propagation of cracks, resulting in a decrease in fatigue life.

It can be seen from Equation (13) that the strain hardening index n' is inversely proportional to the value of SDAS, and the level of n' indicates the material's ability to uniformly deform by hardening before necking occurs, and the degree of hardening under certain conditions. In A319 cast aluminum alloy, eutectic silicon particles and aluminum dendrites are alternately distributed, and continue to interact with dislocations under cyclic loading. In specimens with high cooling rates, the frequency of this interaction is greatly increased, and macroscopically showing a faster hardening rate. Besides, in polycrystalline metals, when grains adjacent undergo plastic deformation, some of the dislocation sources inside the grains will start and slip first, and when they move to the grain boundary, they will be blocked and staged, making fine-grained materials a higher level of hardening. A319 cast aluminum alloy undergoes a certain degree of cyclic hardening under uniaxial and multiaxial fatigue loading, and finally reaches a stable stress amplitude for a given strain amplitude. The non-proportionally additional strengthening factor L_2 represents the degree of increase in the equivalent stress amplitude after multiaxial loading compared with uniaxial loading under the same equivalent strain amplitude. According to the analysis of strain hardening index n', the sample with high cooling rate or Sr modification treatment has a finer microstructure, the stabilized stress amplitude will be farther apart from the uniaxial situation under multiaxial non-proportional fatigue loading and the value of L_2will thus be larger.

Substituting Equation (9-14) into Equation (5), the following complete multiaxial non-proportional fatigue life prediction model is obtained:

$$\frac{\Delta\gamma_{max}}{2}=\left(1+\left(w_1+w_2/SDAS+w_3*¿\varnothing\right)^{-¿¿}\right. \quad (14)$$

Substituting the SDAS and Si particle size of the 6 groups of specimens into the above Equation, the life prediction results are shown in Fig.13. Because of additional fitting of 6 sets of microstructure-based model parameter Equations, the accuracy of multiaxial life prediction is slightly lower than that of the constitutive equation: 56%

of the data points fall within the bound lines of factor of 2, and 83% of the data points fall within the bound lines of factor of 3, high prediction accuracy is still maintained. In addition, from the perspective of loading paths, under the rectangular path, the fatigue life prediction of the material is more aggressive, and the predicted life is higher than the actual life. However, the prediction under the square path and the diamond path is more conservative, and the predicted life is lower than the actual life. It can be seen from Equation (6) that for the same material, the six fatigue parameters are fixed, so the prediction trend of the life model depends on the maximum shear strain amplitude under different non-proportional paths and non-proportionalities. It can be seen from the above prediction results that for A319 cast aluminum alloy, taking the maximum shear strain amplitude and non-proportionality as the fatigue damage parameters, relatively aggressive prediction results will be obtained under the rectangular path, while under the square and diamond paths, the life predictions are conservative.

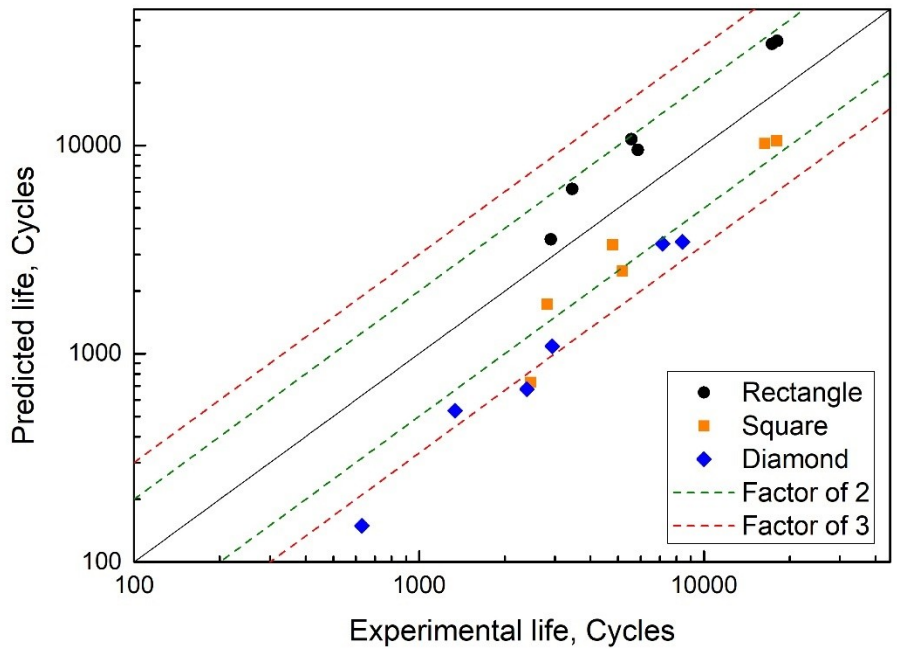

Fig.10 Comparison of predicted lives using micro-based life models with experimental data for 319 under different loading paths.

4. Conclusions

The following conclusions can be drawn from this study:

1. Increasing cooling rate and adding Sr modification in A319 alloy decreases SDAS and improves the morphology and distribution of eutectic Si particles, leading to higher strength and better ductility;
2. The cyclic hardening of A319 aluminum alloy occurs under all three multiaxial non-proportional loading paths (diamond, square and rectangular). After reaching the cyclically stable stage, the stress amplitude under diamond path is the largest, followed by square path and rectangular path.; Six A319 cast aluminum alloys with different microstructure exhibit different stress response characteristics under the same loading conditions. The specimen with higher cooling rate has the maximum stress value after reaching the cyclically stable stage, which reflects the higher resistance of the material to cyclic load. The stress amplitude of materials with the same cooling rate is further increased after Sr modification. There is no obvious difference between the two materials with the lowest cooling rate.
3. The fatigue fracture surface consists of fatigue crack initiation zone, stable growth zone and final fracture zone. In the samples with high cooling rate, the crack initiation area fluctuates slightly, and the fatigue crack initiation source is mostly oxide inclusions near the surface, while the crack initiation in the samples with low cooling rate is mainly due to peeling or fracture of silicon particles near the surface. In the fatigue crack growth area, the silicon particles have different failure modes according to different modification conditions of specimens; The final fracture area surface is drastically rugged, and some oxide inclusions can be observed, which accelerate the final fracture process.

4. The fatigue parameters are fitted by SDAS and Si particle sizes, and the corresponding quantitative relationships are obtained. It can be obtained from the mathematical relationship that the decrease of SDAS and Si particle sizes will lead to the increase of σ_f', $|b_0|$, ε_f', $|c_0|$, n' and L_2, meaning the increase of strength and plasticity, as well as the improvement of cyclic hardening ability and extent of non-proportionally additional strengthening. For the new microstructure-based life prediction model, 56% of the data points fall in the bound lines of factor of 2, and 83% of the data points fall in the bound lines of factor of 3; The prediction results under the rectangular path are higher than the actual life, while the predicted lives of the square path and diamond paths are more conservative and lower than the actual lives.

Acknowledgement

The authors would like to express sincere thanks to General Motors (Project No. 1314) for the materials and financial support.

References

1. Le P, Liu X, He G, Ge B, Wang Q. Effect of HIPing and degassing on the low cycle fatigue behavior of A319 cast alloy. *Mater Sci Eng A*, 2019; 6(10):106552-.
2. Emami AR, Begum S, Chen DL, Skszek T, Niu XP, Zhang Y, Gabbianelli F. Cyclic deformation behavior of a cast aluminum alloy. *Mater Sci Eng A*. 2009; 516(1-2): 31-41.
3. Liu XS, He GQ, Ding X, Mo DF, Zhang WH. Fatigue behavior and dislocation substructures for 6063 aluminum alloy under nonproportional loadings. *Int J Fatigue*. 2009; 31(7): 1190-1195.
4. Tian DD, Liu XS, He GQ, Shen Y, Lv SQ, Wang QG. Low cycle fatigue behavior of casting A319 alloy under two different aging conditions. *Mater Sci Eng A*. 2016; 654: 60-68.
5. Dispinar D, Campbell J. Effect of casting conditions on aluminium metal quality. *J Mater Process Technol*. 2007; 182(1-3): 405-410.m

6. Haskel T, Verran GO, Barbieri R. Rotating and bending fatigue behavior of A356 aluminum alloy: Effects of strontium addition and T6 heat treatment. *Int J Fatigue*. 2018; 114: 1-10.
7. Tenkamp J, Koch A, Knorre S, Krupp U, Michels W, Walther F. Defect-correlated fatigue assessment of A356-T6 aluminum cast alloy using computed tomography based Kitagawa-Takahashi diagrams. *Int J Fatigue*, 2018; 108(mar.):25-34.
8. Kumai S, Aoki S, Han S-W, Sato A. Effects of Dendrite Cell Size and Eutectic Si Particle Morphology on Fatigue Crack Growth in Cast and HIPed AC4CH Alloys. *Mater Trans, JIM*. 1999; 40(7): 685-691.
9. Lu SZ , Hellawell A . The mechanism of silicon modification in aluminum-silicon alloys: Impurity induced twinning. *Metall. Trans. A*, 1987; 18(10):1721-1733.
10. Huiyuan G, Yanxiang L, Xiang C, Xue W. Effects of boron on eutectic solidification in hypoeutectic Al–Si alloys. *Scripta Mater*, 2005; 53(1):69-73.
11. Conley JG, Huang J, Asada J, Akiba KJMS, A E. 2000. Modeling the effects of cooling rate, hydrogen content, grain refiner and modifier on microporosity formation in Al A356 alloys. *Mater Sci Eng A*, 285(1): 49-55.
12. Gall K, Horstemeyer MF, Degner BW, Mcdowell DL, Fan J. On the driving force for fatigue crack formation from inclusions and voids in a cast A356 aluminum alloy. *Int J Fract*, 2001; 108(3):207-233.
13. Le VD, Morel F, Bellett D, Pessard E, Saintier N, Osmond P. Microstructural-based analysis and modelling of the fatigue behaviour of cast Al-Si alloys. *Procedia Eng*, 2015; 133:562-575.
14. Wang Q G , Apelian D , Lados DA. Fatigue behavior of A356-T6 aluminum cast alloys. Part I. Effect of casting defects. *J Light Met*, 2001; 1(1):73-84.
15. Wang QG, Apelian D, Lados DA. Fatigue behavior of A356/357 aluminum cast alloys. Part II – Effect of microstructural constituents. *J Light Met*. 2001; 1(1): 0-97.
16. Houria MI, Nadot Y, Fathallah R, Roy M, Maijer DM. Influence of casting defect and SDAS on the multiaxial fatigue behaviour of A356-T6 alloy including mean stress effect. *Int J Fatigue*. 2015; 80(nov.):90-102.
17. Manson S S . Fatigue: A complex subject—Some simple approximations. *Exp Mech*. 1965; 5(7):193-226.
18. Ellyin F, Golos K. Multiaxial Fatigue Damage Criterion. *J Eng Mater-T*. 1988; 110(1):63.
19. Garud YS . A New Approach to the Evaluation of Fatigue Under Multiaxial Loadings. *J Eng Mater-T ASME*. 1981; 103(2):118-125.
20. Brown MW,Miller KJ. A Theory for Fatigue Failure under Multiaxial Stress-Strain Conditions. *P I Mech Eng*. 2016; 187(1):745-755.
21. Socie DF . Multiaxial Fatigue Damage Models. *J Eng Mater-T ASME*. 1987, 109(4):293.
22. He GQ. Effect of material microstructure on low cycle fatigue characteristics under uniaxial and multiaxial non-proportional loading[D].
23. Ge B, Liu X, He G, Le P. Wen Z, Wang Q. Quantitative relationship between microstructure characteristics and fatigue parameters of A319 casting alloy. *Fatigue Fract Eng Mater Struct*. 2020; 43(3).
24. Song MS, Kong YY, Ran MW, Ran MW, She YC. Cyclic stress–strain behavior and low cycle fatigue life of cast A356 alloys. *Int J Fatigue*. 2011; 33(12):1600-1607.